

## Article

# In Situ Ni-Doped Hierarchically Porous Carbon Nanofibers Derived from Polyacrylonitrile/Pitch for Hydrogen Storage at Ambient Temperature

Fuquan Song<sup>1,2,\*</sup> , Lintao Huang<sup>2</sup>, Heying Ding<sup>2</sup>, Shiming Zhang<sup>3</sup> and Jinbiao Yu<sup>3</sup><sup>1</sup> School of Petroleum and Natural Gas Engineering, Changzhou University, Changzhou 213164, China<sup>2</sup> School of Petrochemical Engineering and Environment, Zhejiang Ocean University, Zhoushan 316022, China<sup>3</sup> Exploration and Development Research Institute, Shengli Oilfield Company, SINOPEC, Dongying 257015, China

\* Correspondence: songfuquan@cczu.edu.cn

**Abstract:** Porous carbon nanofibers doped with nickel (Ni) were successfully fabricated through electrospinning, carbonization, and CO<sub>2</sub> activation techniques using polyacrylonitrile (PAN) and petroleum pitch as carbon sources and nickel acetate as the dopant. During the activation process, Ni was reduced and dispersed in situ on the carbon matrix. The effects of Ni doping content on the morphology and structure of the carbon nanofibers were systematically investigated using SEM, TEM, XPS, XRD, Raman, and BET analyses. The experimental results revealed that the prepared materials had a hierarchically porous structure and that Ni nanoparticles played multiple roles in the preparation process, including catalyzing pore expansion and catalytic graphitization. However, particle agglomeration and fiber fracture occurred when the Ni content was high. In the adsorption/desorption experiments, the sample with 10 wt% Ni doping exhibited the highest specific surface area and micropore volume of 750.7 m<sup>2</sup>/g and 0.258 cm<sup>3</sup>/g, respectively, and had the maximum hydrogen storage capacity of 1.39 wt% at 298 K and 10 MPa. The analyses suggested that the hydrogen adsorption mechanism contributed to enhanced H<sub>2</sub> adsorption by the spillover effect in addition to physisorption.

**Keywords:** carbon nanofiber; petroleum pitch; electrospinning; hydrogen adsorption; spillover

**Citation:** Song, F.; Huang, L.; Ding, H.; Zhang, S.; Yu, J. In Situ Ni-Doped Hierarchically Porous Carbon Nanofibers Derived from Polyacrylonitrile/Pitch for Hydrogen Storage at Ambient Temperature. *Sustainability* **2023**, *15*, 8722. <https://doi.org/10.3390/su15118722>

Academic Editors: Sagar Shirsath, Sumanta Kumar Karan and Bhanu Bhusan Khatua

Received: 24 April 2023

Revised: 16 May 2023

Accepted: 20 May 2023

Published: 29 May 2023



**Copyright:** © 2023 by the authors. Licensee MDPI, Basel, Switzerland. This article is an open access article distributed under the terms and conditions of the Creative Commons Attribution (CC BY) license (<https://creativecommons.org/licenses/by/4.0/>).

## 1. Introduction

The demand for global energy has continued to rise, and energy and environmental issues have become increasingly important worldwide. Conventional fossil fuels produce large amounts of greenhouse gases, such as CO<sub>2</sub>, which contribute to global warming. To mitigate the effects of climate change and address concerns about energy security, it is crucial to develop new energy sources that can replace fossil fuels. Hydrogen (H<sub>2</sub>) is an ideal clean energy source that produces no carbon emissions during combustion and only water as a byproduct. It is also the most abundant element in the universe, making it a rich source for H<sub>2</sub> production [1–5]. Moreover, hydrogen has a higher gravimetric energy density than hydrocarbon fuels such as gasoline and kerosene [6]. As a result, hydrogen energy has become a hot topic in the global energy field and is considered a feasible technology for promoting the global energy transition. European and American governments, as well as important international organizations such as the International Energy Agency, have high expectations for the hydrogen energy economy [7].

The volumetric energy density of hydrogen is quite low compared to that of gasoline or other hydrocarbons, although hydrogen has a high gravimetric energy density [6]. This greatly limits the efficient utilization of hydrogen energy, as the volume of 1 kg H<sub>2</sub> is about 11,250 L at atmospheric temperature and pressure, and the volumetric energy density of compressed hydrogen (4.7 MJ/L) at 70 MPa is only about one-sixth of that of gasoline

(31.7 MJ/L). Thus, the safe and efficient storage and transportation of hydrogen at ambient temperature and pressure is the biggest challenge for hydrogen energy technology, and how to store hydrogen safely and tightly is the key to its application.

Currently, research on hydrogen storage mainly focuses on improving hydrogen energy density, with methods including (i) compressed hydrogen; (ii) liquefied hydrogen; (iii) chemical hydrogen storage (e.g., metal hydrides or other hydrogen-containing compounds); and (iv) physical adsorption (i.e., adsorption on materials with a high surface area) [8]. Compressed hydrogen, which requires a high-pressure vessel (up to 70 MPa), is the most commonly used method of hydrogen storage. However, this method has a low hydrogen storage density (only 39.1 kg/m<sup>3</sup> at 70 MPa) and requires a high storage vessel [9]. Liquefied hydrogen has a high storage density (0.071 kg/L), but it needs to be stored at an ultra-low temperature of 20 K and requires a high level of adiabatic capacity for the storage tank used, and the energy consumed in this process is about 25~45% of the stored hydrogen energy. Therefore, it is mostly used in the aerospace industry at present [6,10].

In recent years, adsorbent materials have been widely studied for hydrogen storage as a potential solution to the limitations of other storage methods. Among these materials, carbon-based materials have gained significant attention due to their simple preparation process, cost-effectiveness, high specific surface area, and fast desorption speed [11]. Various carbon materials have been explored for hydrogen storage, including activated carbon [12,13], carbon nanotubes [14], carbon aerogels [15], and carbon nanofibers [16–18]. The hydrogen storage capacity of these materials depends on their physicochemical properties. For instance, carbon nanotubes have hydrogen adsorption sites mainly on their internal/external surface and interplanar spacing, with multi-walled carbon nanotubes having an advantage over single-walled carbon nanotubes for hydrogen storage [19,20]. Moreover, Browning et al. proposed that hydrogen adsorption on carbon nanofibers involves a slow chemisorption process, where the rate of hydrogen adsorption is determined by the rate of hydrogen dissociation on graphite edge sites, and the dissociated hydrogen atoms subsequently migrate into the graphite sheets before adsorbing on the carbon nanofiber surface [21].

Relevant studies on hydrogen storage in carbon-based materials have mainly focused on low-temperature conditions, specifically at liquid nitrogen temperature (77 K), while less attention has been paid to the hydrogen storage performance at ambient temperature. Musyoka et al. [22] synthesized activated carbon with high microporosity from unburned fly ash with high carbon content, which exhibited a hydrogen storage capacity of 1.35 wt% at 77 K and 1 bar. Sevilla et al. [23] obtained activated carbons with ultra-high specific surface areas (3000~3500 m<sup>2</sup>/g) by chemically activating polypyrrole as a carbon precursor with KOH and showed a maximum hydrogen adsorption capacity of 7.03 wt% (77 K, 20 bar). Moreover, the hydrogen storage capacity of carbon materials can be improved by adding transition metals to the carbon matrix via the hydrogen spillover mechanism. Kim et al. [24] prepared PAN-based palladium-coated porous carbon nanofibers through co-electrospinning and experimentally evaluated their hydrogen storage performance in the presence of Pd particles. The results showed that the hydrogen adsorption capacity of Pd-coated carbon nanofibers was 0.82 wt% at 298 K and 0.1 MPa, with hydrogen spillover contributing 0.23 wt% H<sub>2</sub>. Computational and simulation studies have also shown that transition metal atoms can act as active sites for H<sub>2</sub> dissociation and hydrogen spillover while reducing the energy barrier for H<sub>2</sub> dissociation [25].

Among the various raw materials for synthesizing carbon materials, petroleum pitch is undoubtedly one of the cheapest. It is a waste by-product of crude oil refining that offers several advantages, including easy graphitization, high carbon yield, and low cost compared to polyacrylonitrile [26]. In addition, electrospinning is a widely adopted method for fabricating nanofibers, and it stands out as a simple, versatile, and scalable technique specifically for fabricating carbon nanofibers. One of the notable advantages of electrospinning is its capability to adjust various parameters, including solution concentration, flow

rate, and applied voltage, to produce nanofibers with specific diameters, surface areas, and porosity, catering to the desired properties and applications [27,28].

This study aims to fabricate hierarchically porous carbon nanofibers with well-dispersed nickel nanoparticles using electrospinning and to investigate their hydrogen storage performance at ambient temperature. Specifically, this study: (1) synthesizes nickel-doped porous carbon nanofibers from polyacrylonitrile and petroleum pitch as carbon sources and nickel acetate as dopant; (2) characterizes the morphology, structure, chemical composition, and pore texture of the prepared materials by various techniques; (3) evaluates the hydrogen adsorption/desorption properties of the prepared materials at 298 K and different pressures by PCT method and compares them with undoped samples; (4) analyzes the effect of nickel doping content on the pore structure and hydrogen storage performance of porous carbon nanofibers and explores the possible adsorption mechanism involving physical adsorption and spillover effect. This study provides a feasible strategy for the fabrication of carbon-based materials for room-temperature hydrogen storage and contributes to the development of clean energy technology. The novelties of this study include the use of petroleum pitch as a carbon source and the multiple roles of Ni particles in pore expansion, catalytic graphitization, and enhanced H<sub>2</sub> adsorption.

## 2. Experiments

### 2.1. Materials and Fabrication

All chemicals were obtained commercially and used without any purification. Petroleum pitch was bought from Dalian Mingqiang Chemical Materials Co., Ltd. (Dalian, China). Polyacrylonitrile (PAN) with molecular weight of 150,000 g/mol, nickel acetate tetrahydrate (Ni(Ac)<sub>2</sub>·4H<sub>2</sub>O) and N, N-dimethylformamide (DMF) were both purchased from Sinopharm Chemical Reagent Co., Ltd. (Shanghai, China). Tetrahydrofuran (THF) was obtained from Shanghai Macklin Biochemical Co., Ltd. (Shanghai, China).

PAN and petroleum pitch were used as carbon sources, DMF and THF were used as solvents, and nickel acetate tetrahydrate was used as the dopant. The homogeneous spinning solution for electrospinning was prepared by adding the solution of pitch in THF to PAN in DMF solution to achieve a mixed solution with a PAN/pitch weight ratio of 75/25 wt%, and then a given amount of Ni(Ac)<sub>2</sub>·4H<sub>2</sub>O was added to it and magnetic stirring was performed at room temperature for 8 h. After that, the prepared precursor solution was injected into a syringe with a 0.6 mm inner diameter flat needle, and the PAN/pitch/Ni(Ac)<sub>2</sub> spinning solution was electrospun into nanofibers using an electrospinning device (SNZJ-1400, Qingdao Sibeining Intelligent Equipment Co., Ltd., Qingdao, China), and the corresponding spinning parameters were set as follows: flow rate of 0.6 mL/h, applied voltage of 15 kV, and tip-to-collector distance of 13 cm. The prepared electrospun nanofibers were heated from room temperature to 250 °C in a muffle furnace at a heating rate of 2 °C/min and maintained for 90 min to obtain the pre-oxidized precursor. Finally, a tube furnace was used to carbonize at 900 °C in a nitrogen atmosphere for 1 h at a heating rate of 5 °C/min, and subsequent activation was carried out in a CO<sub>2</sub> atmosphere for 30 min. The target products obtained were noted as ACNF, ACNF-1, ACNF-2, and ACNF-3 according to the weight ratio of nickel acetate (0, 10, 20, and 30 wt%), respectively (Figure 1).

### 2.2. Characterizations

The microstructure and surface morphology of samples were examined using a field emission scanning electron microscope (FE-SEM, Hitachi S4800, Hitachi Ltd., Tokyo, Japan) equipped with an energy dispersive spectroscopy (EDS) at an accelerated voltage of 5 kV, and the fiber diameters in the SEM images were measured using Image J software (V1.8.0.112). The lattice striations and Ni particle size of the samples were further observed by transmission electron microscopy (TEM, JEM-2100F, JEOL Ltd., Tokyo, Japan). The crystal structure of the samples was analyzed by X-ray diffraction (XRD, Bruker D2 Phaser, Bruker Corporation, MA, USA), and Raman analysis (Thermo Scientific DXR, Thermo

Fisher Scientific Inc., MA, USA) was employed to investigate the relative graphitic characteristics of the samples. The surface chemical state of prepared samples was detected by X-ray photoelectron spectroscopy (XPS, Thermo Scientific K-Alpha, Thermo Fisher Scientific Inc., MA, USA) with an Al K $\alpha$  X-ray source (12 kV, 6 mA). The specific surface area of the samples was determined according to the Brunauer–Emmett–Teller (BET) method using a fully automated surface area and pore size analyzer (Autosorb iQ-3, Anton Paar GmbH, Graz, Austrian) at liquid nitrogen temperature for nitrogen adsorption/desorption testing. The hydrogen adsorption of the prepared material was performed by the PCT method employing an automatic high-pressure gas sorption analyzer (BSD-PH, BeiShiDe Instrument, Beijing, China) at 298 K and a hydrogen pressure range of 0–10 MPa. All samples were degassed in a vacuum degassing station for 3 h at 300 °C before the adsorption analysis. The purity of all gases used for adsorption analysis was 99.999%.

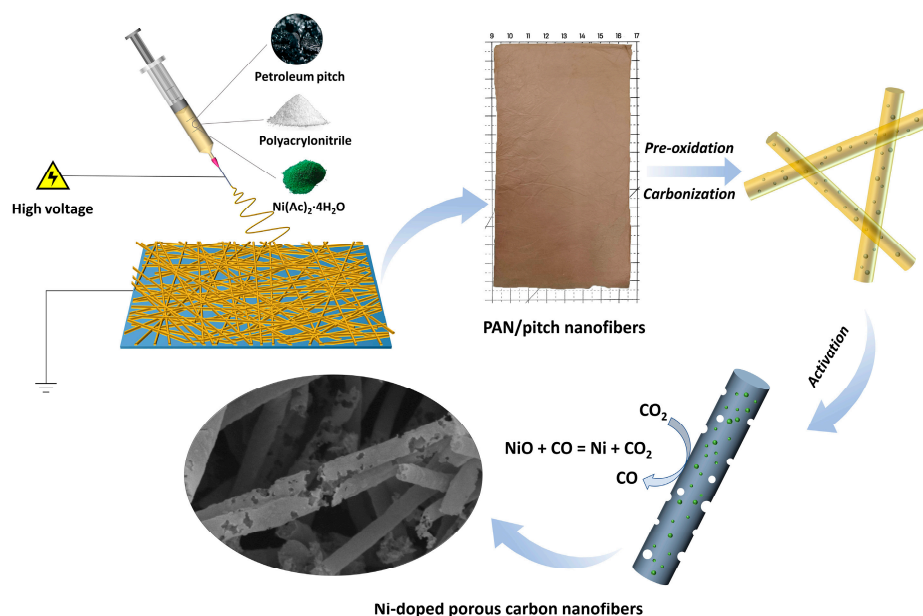


**Figure 1.** The schematic illustration of the fabrication of Ni-doped porous carbon nanofibers.

### 3. Results and Discussion

The microstructure and surface morphology of the samples were characterized by FE-SEM, and the elemental distribution in the samples was analyzed by EDS elemental mapping. Figure 2a–d show the high-magnification SEM images of ACNF, ACNF-1, ACNF-2, and ACNF-3, respectively. The results of fiber diameters and their distribution analysis show that the fiber diameter of all samples is approximately 200 nm, which indicates that the doping of Ni has no obvious effect on the diameter of carbon nanofibers. As for the surface morphology, the surface of the ACNF sample is almost impossible to observe the obvious pore structure (Figure 2a), while abundant pore structures appear in other samples. In ACNF-2 and ACNF-3, especially, both the inside and the surface of the fiber possess an inhomogeneous pore structure, and the carbon fiber is also fractured to varying degrees. Figure 2e,f are the EDS elemental mapping images of ACNF-3 as well as the corresponding spectra. The results indicate that ACNF-3 is mainly composed of C, N, Ni, and O elements, and the weight percentage of Ni nanoparticles dispersed on the surface of the sample is 16.87%. It can thus be deduced that the introduction of nickel during the heat treatment can enrich the pore structure of carbon nanofibers, thereby providing more active sites and radial diffusion channels for hydrogen adsorption [18]. However, the high doping content of Ni in the sample will also lead to interparticle agglomeration, thus reducing the adsorption/desorption performance of hydrogen [29]. Figure 3 shows the TEM images of ACNF-3 at different resolutions. It is obvious from Figure 3a,b that the fiber surface is rough and porous, and the Ni nanoparticles anchored in the fiber with their diameter

ranging from 10 to 40 nm. In the high-resolution TEM images of ACNF-3 (Figure 3c,d), the lattice spacing of about 0.356 nm corresponds to the (002) planes of graphitic carbon, suggesting the amorphous carbon is partially converted to graphitic carbon.

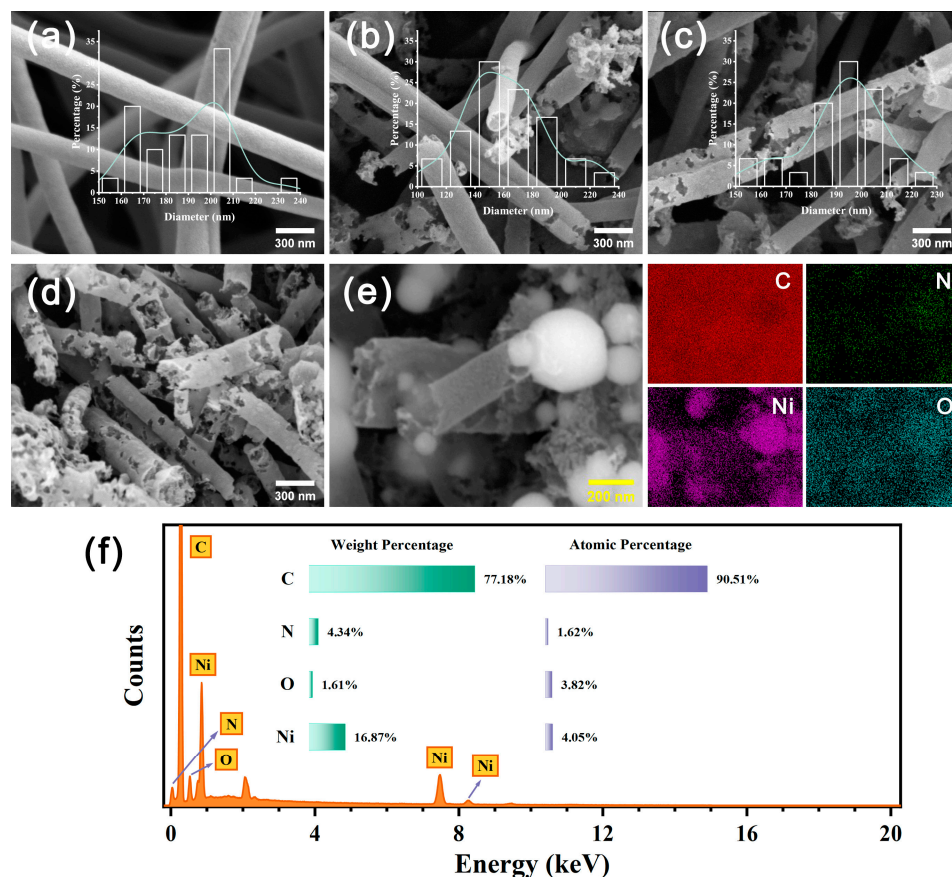


**Figure 2.** FE-SEM images of (a) ACNF, (b) ACNF-1, (c) ACNF-2, (d) ACNF-3, and (e,f) EDS elemental mapping images and EDS spectra.

The surface chemical structure as well as the valence states of elements for ACNF and ACNF-3 were further analyzed by X-ray photoelectron spectroscopy (XPS). XPS results clearly exhibited signals of C, N, and O elements in all samples, and the presence of Ni was detected in the composition of ACNF-3 (Figure 4a). The Ni atomic content of ACNF-3 was approximately 1.08 at.%, and its C content (92.48 at.%) was slightly higher than that of ACNF (91.18 at.%). The high-resolution C 1s spectrum of ACNF-3 (Figure 4b) could be deconvoluted into three sub-peaks, which were C=C and C-C (184.2 eV), C-O, C-N, and C=N (285.2 eV), and O-C=O (289.2 eV) [30–32]. The deconvolution for the N 1s spectrum of ACNF revealed that the nitrogen species were mainly pyridinic-N (397.9 eV), pyrrolic-N (398.7 eV), and graphitic-N (400.4 eV) [33], and pyridinic-N as well as graphitic-N also existed in ACNF-3 (Figure 4c). For nitrogen-containing carbon materials, it has been generally recognized that the introduction of pyridinic-N into the carbon skeleton can interact with the loaded active metal to enhance binding energy between metal particles and the carbon skeleton, which has a positive effect on hydrogen adsorption [32,34]. As shown in Figure 4d, in the high-resolution Ni 2p spectrum of ACNF-3, two dominant peaks are observed at 853.1 eV and 870.6 eV with a spin-orbit splitting of 17.5 eV, which are attributed to Ni 2p<sub>3/2</sub> and Ni 2p<sub>1/2</sub> of metallic Ni, respectively. Similarly, the peaks at 856.2 eV and 874.6 eV are assigned to the oxidized state of Ni, while the two shake-up peaks at 860.9 eV and 879.3 eV correspond to its satellite peaks [35–37].

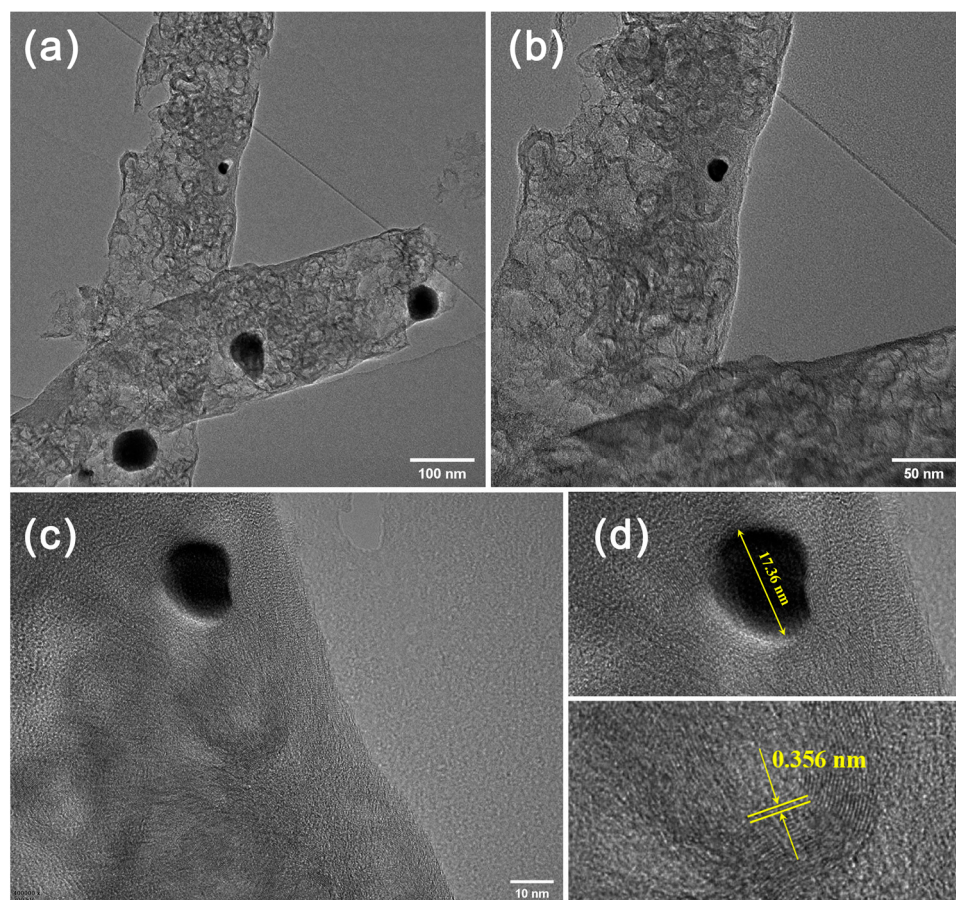


**Figure 3.** (a,b) TEM images and (c,d) high-resolution TEM images of ACNF-3.

The crystallographic plane and crystallite size of the samples were analyzed by wide-angle XRD technique, and the corresponding XRD patterns are shown in Figure 5a. A common diffraction peak at  $2\theta$  angle of  $\sim 25^\circ$  was observed in all samples, which corresponded to the crystal plane (002) of the amorphous carbon [38]. It is not hard to perceive that the broad diffraction peak at  $\sim 23^\circ$  is red-shifted to a sharp diffraction peak at  $\sim 26^\circ$  as the nickel content increases, and the corresponding interlayer spacing ( $d_{002}$ ) of the samples calculated by the Bragg equation decreases from 0.385 nm to 0.342 nm, indicating that the nickel doping improves the graphitization degree of the carbon matrix to a certain extent [17,39]. Moreover, the diffraction peaks observed at  $2\theta$  angles of  $44.5^\circ$ ,  $51.8^\circ$ , and  $76.4^\circ$  correspond to the (111), (200), and (220) crystal planes of Ni (JCPDS No.04-0850), respectively. This reveals that the Ni species on the surface of the carbon matrix exist in metallic form, and the crystallite size of Ni nanoparticles was calculated according to the Scherrer equation ranging from 35.8 nm for ACNF-1 to 42.8 nm for ACNF-3 [19,40]. The oxidation state of Ni determined in the previous XPS analysis did not observe the corresponding characteristic peaks here. It could be due to the fact that the NiO exposed on the surface of the carbon matrix was reduced to metallic Ni by the CO generated during the  $\text{CO}_2$  activation, while the NiO present inside it could not be detected by the instrument. This also further confirms that metal nanoparticles move to form pores during the activation process [41].

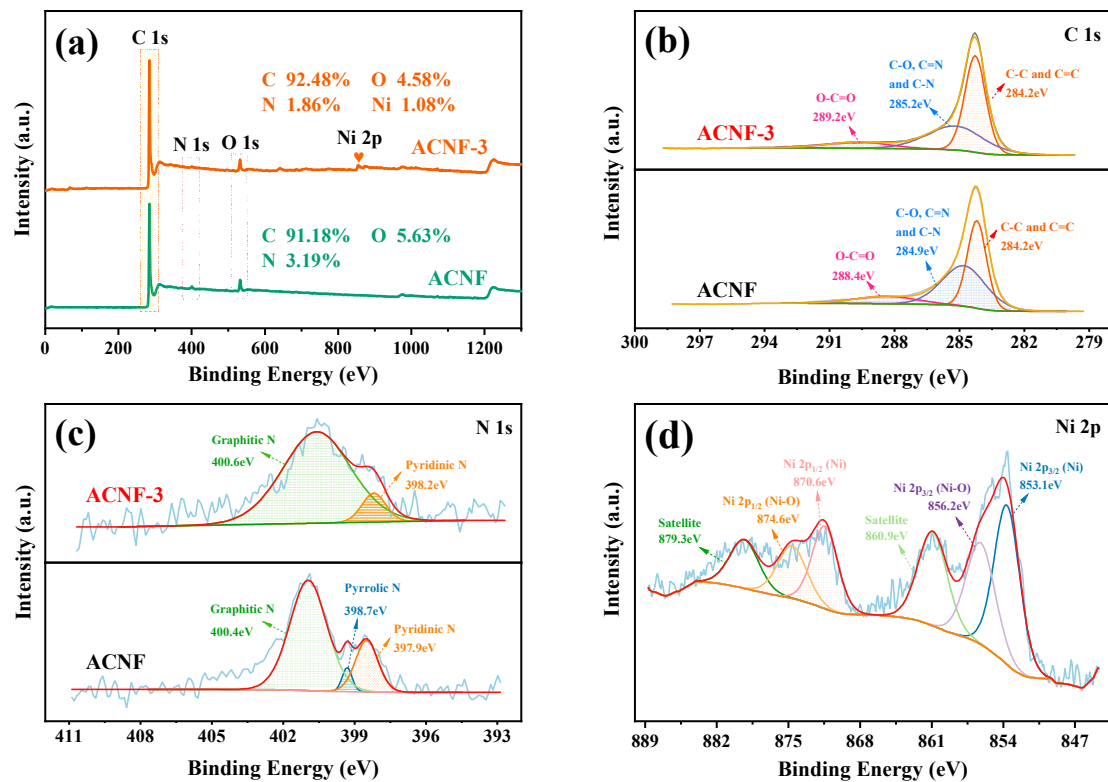


**Figure 4.** (a) XPS surveys of ACNF and ACNF-3, (b) high resolution C 1s XPS spectra, (c) high resolution N 1s XPS spectra, and (d) high resolution Ni 2p XPS spectra of ACNF-3.

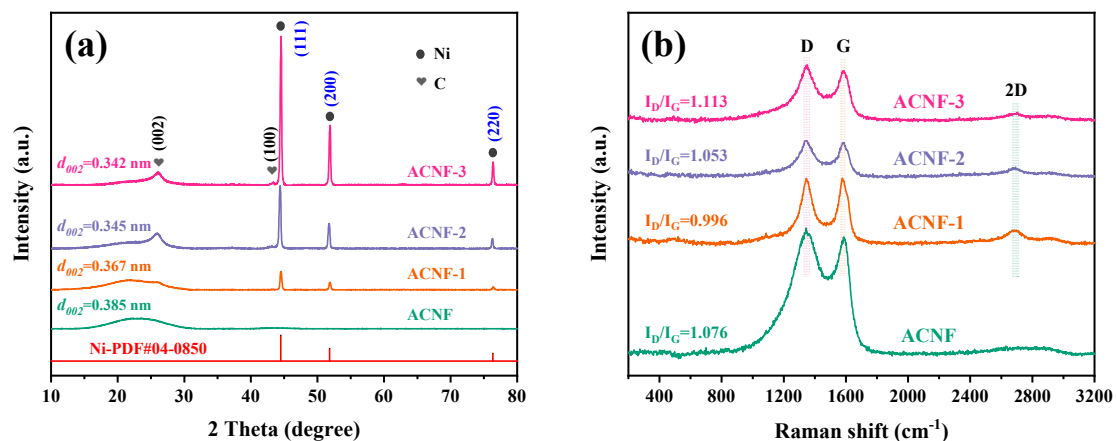


**Figure 5.** (a) XRD patterns and (b) Raman spectra of ACNF, ACNF-1, ACNF-2, and ACNF-3.

To further investigate the structural defects of carbon and disordered graphite structure in ACNFs, Raman analysis was performed on the samples. As can be seen in Figure 5b, all samples show two distinct characteristic peaks at  $1350\text{ cm}^{-1}$  and  $1580\text{ cm}^{-1}$ , corresponding to the D and G bands, respectively, while other samples except ACNF possess a slight 2D band at around  $2700\text{ cm}^{-1}$ . Typically, the D band at  $1350\text{ cm}^{-1}$  is associated with structural defects of  $sp^3$  hybridized carbon atoms and reflects the disordered graphite structure, whereas the G band at  $1580\text{ cm}^{-1}$  is related to  $sp^2$  carbon atoms and the 2D band represents the interlayer stacking order of carbon atoms in the sample [35,42]. The intensity ratio,  $R (I_D/I_G)$ , between the D and G bands reveals the relative degree of disorder in the carbon materials, and the lower the R-value, the higher the degree of graphitization of the carbon material [43]. The Raman spectra of ACNF-1 have the minimum R-value, as was also confirmed by the XRD analysis discussed above. Subsequently, the further

increase in Ni doping content also leads to the increase in R-value, which may be due to the excessive nickel entering inside the carbon matrix and hindering the construction of the carbon hexagonal network, thus resulting in a decrease in graphitization [44,45].

The nitrogen adsorption/desorption isotherms of the sample and the corresponding pore size distribution are shown in Figure 6. It can be seen from Figure 6a that the  $N_2$  adsorption/desorption isotherms of all samples exhibit high adsorption capacities at a low relative pressure ( $P/P_0 < 0.1$ ), indicating the presence of micropores in the samples. The isotherms of ACNF samples correspond to type I according to the IUPAC classification [46]. By contrast, ACNF-1, ACNF-2, and ACNF-3 present a type IV isotherm with obvious type H3-type hysteresis loops, suggesting that the three samples possess a hierarchically porous structure, which implies the existence of micropores, mesopores, and macropores [47,48]. The difference in pore structure of the samples could be further revealed by the pore size distribution calculated by the NLDFT (non-local density functional theory) method. As can be seen in Figure 6b, most of the pores in ACNF and ACNF-1 are micropores below 2 nm. Compared with ACNF, ACNF-1 has a considerable number of mesopores with pore sizes between 3.5 and 4.5 nm. As for ACNF-2 and ACNF-3, except for some micropores, the pore sizes are shifted towards larger pores and are predominantly mesoporous.

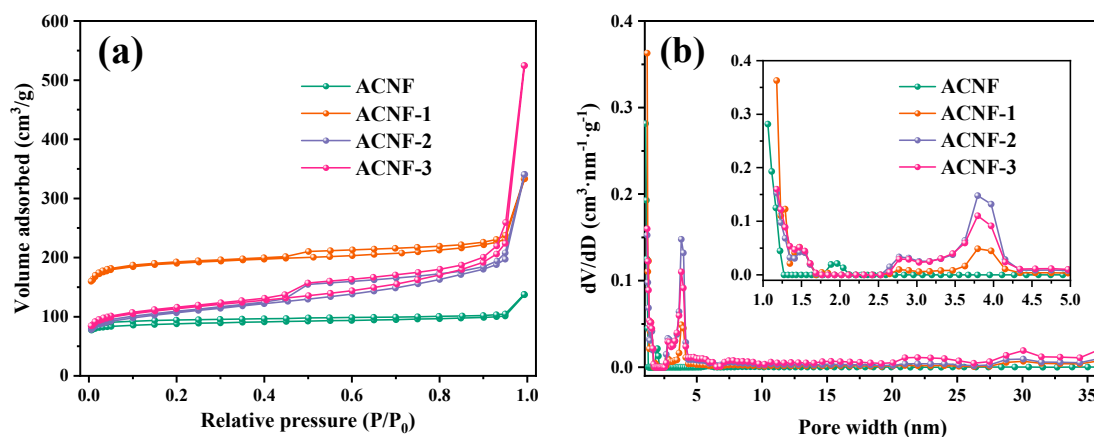


**Figure 6.** (a) Nitrogen adsorption/desorption isotherms and (b) pore size distributions of ACNF, ACNF-1, ACNF-2, and ACNF-3.

The specific surface area and pore texture parameters of the samples are shown in Table 1, and the specific surface area was calculated by the Brunauer–Emmett–Teller (BET) equation. Compared with ACNF, the specific surface area and pore volume of ACNF-1 increased to  $750.7 \text{ m}^2/\text{g}$  and  $0.515 \text{ cm}^3/\text{g}$ , respectively, indicating that the in situ doped Ni nanoparticles played a significant catalytic role in pore expansion during the activation process [41]. The subsequent increase in pore size with increasing Ni content also confirmed this. However, the excessive doping of nickel also led to the blockage of pore channels in the as-prepared sample, which reduced its specific surface area. Therefore, an appropriate proportion of Ni nanoparticles contributed to increasing the specific surface area and micropore volume, and a higher specific surface area and micropore volume were beneficial for its application in hydrogen storage [49].

Figure 7b displays the hydrogen adsorption isotherms of the prepared material at 298 K and 0–10 MPa. In the absence of Ni nanoparticle doping, hydrogen molecules are adsorbed in the micropores and slits of the porous carbon by van der Waals forces. It has been reported that the hydrogen storage capacity of porous carbon materials is not totally dependent on the specific surface area of the materials themselves, and hydrogen adsorption at high pressure also strongly depends on the pore size of the materials [50]. The kinetic diameter of hydrogen molecules is 0.4059 nm, and hydrogen molecules can be effectively captured when the pore width is 0.6–0.7 nm [51], while nanopores with a size of 1.5–2.5 nm can also provide diffusion pathways and storage space for hydrogen

molecules [49]. As for Ni-doped porous carbon materials, hydrogen adsorption occurs in the material via the spillover effect, that is, the hydrogen molecules on the surface of the Ni nanoparticles are dissociated into hydrogen atoms and migrate to the micropore channels of the porous carbon, thereby improving the hydrogen adsorption capacity of the materials [19,38] (Figure 7a). Among the prepared porous carbons, ACNF-1 exhibited the highest hydrogen adsorption capacity, with a high hydrogen adsorption capacity of 1.39 wt% at 298 K and 10 MPa, mainly due to the high microporous specific surface area associated with narrow micropores (0.6~0.7 nm) of ACNF-1 [52].

**Table 1.** Pore structure parameters and hydrogen storage of samples.

Sample	$S_{\text{BET}}^{\text{a}}$ ( $\text{m}^2/\text{g}$ )	$V_{\text{total}}^{\text{b}}$ ( $\text{cm}^3/\text{g}$ )	$S_{\text{micro}}^{\text{c}}$ ( $\text{m}^2/\text{g}$ )	$V_{\text{micro}}^{\text{d}}$ ( $\text{cm}^3/\text{g}$ )	$D^{\text{e}}$ (nm)	$\text{H}_2$ Uptake $^{\text{f}}$ (wt%)
ACNF	347.1	0.213	308.8	0.120	2.5	0.60
ACNF-1	750.7	0.515	666.8	0.258	2.7	1.39
ACNF-2	387.7	0.527	218.3	0.092	5.3	0.85
ACNF-3	415.8	0.811	245.4	0.101	7.8	0.66

<sup>a</sup>  $S_{\text{BET}}$ : BET specific surface area. <sup>b</sup>  $V_{\text{total}}$ : total pore volume. <sup>c</sup>  $S_{\text{micro}}$ : micropore surface area, calculated by the t-plot method. <sup>d</sup>  $V_{\text{micro}}$ : micropore volume, determined by the Horvath–Kawazoe (HK) method. <sup>e</sup>  $D$ : average pore width. <sup>f</sup>  $\text{H}_2$  uptake: hydrogen uptake capacity at 298 K and 10 MPa.

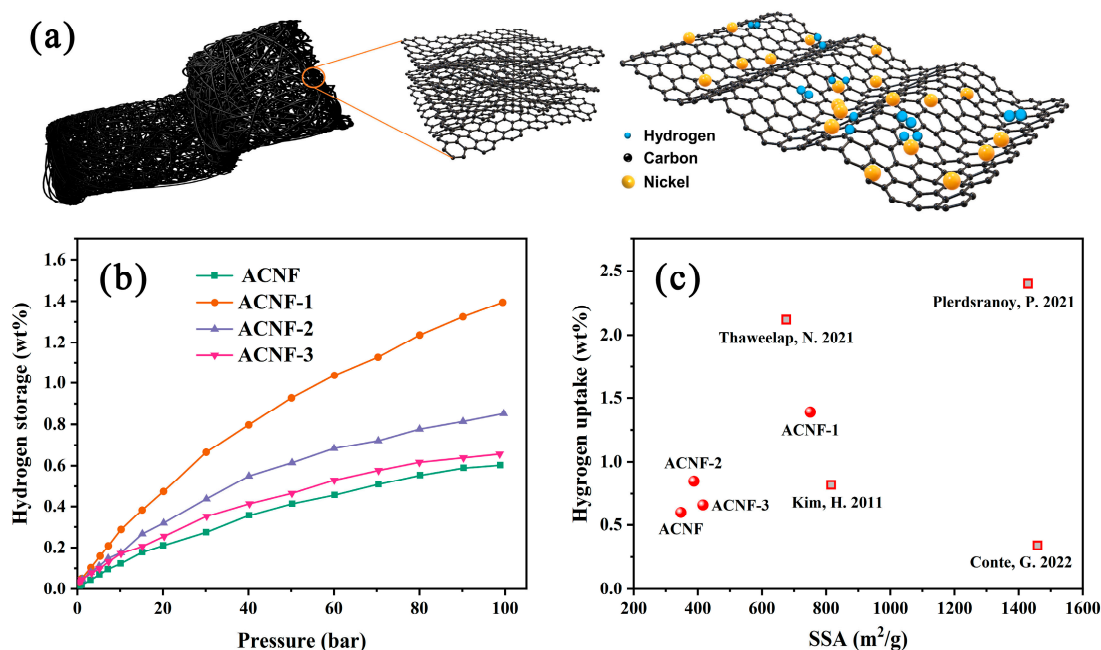


**Figure 7.** (a) Schematic illustration of hydrogen spillover mechanism on Ni-dispersed carbon nanofibers, (b) hydrogen adsorption isotherms of ACNFs at 298 K, and (c) comparison with hydrogen storage capacity of carbon-based materials (measured at 298 K, 10 MPa) [24,29,32,53].

According to the Chahine rule, the hydrogen adsorption capacity on porous carbon is approximately 1 wt%  $\text{H}_2$  per 500  $\text{m}^2/\text{g}$  of the surface area at 77 K and 20 bar [54,55]. Considering that the hydrogen storage temperature employed in this study is 298 K, it is necessary to carry out a systematic analysis in conjunction with the data reported in related studies (Figure 7c). In a similar manner to the Chahine rule, the hydrogen adsorption capacity per unit specific surface area of pure porous carbon can be estimated as  $1.73 \times 10^{-3}$  wt% at 298 K [56]. Based on this calculation, the theoretical hydrogen adsorption capacity was determined to be 1.29 wt%. Thus,  $\sim 0.1$  wt% of hydrogen was dissociated and accumulated on the interface between the Ni nanoparticle–carbon matrix via the spillover effect during the adsorption process.

In addition, a comparison of the hydrogen storage performance of comparable adsorbents (as shown in Table 2) reveals the conclusion that low temperature and high pressure are necessary to improve the hydrogen storage capacity of the materials. Furthermore, elemental doping and increasing the specific surface area (particularly the specific surface area of micropores) are also effective methods for improving the hydrogen adsorption performance of carbon-based materials. The hydrogen storage capacity of Ni-doped porous carbon materials prepared in this study is comparable to or even better than some high specific surface area adsorbents listed in the table, which is of great significance for the subsequent research on materials with higher hydrogen storage performance.

**Table 2.** A comparison of hydrogen adsorption capacity of various materials.

Absorbents	$S_{\text{BET}}$ (m <sup>2</sup> /g)	Condition		H <sub>2</sub> Uptake (wt%)	References
		Temp. (K)	Pres. (bar)		
Cu-impregnated AC	1459	298	80	0.34	[53]
Ni-doped MWNCT	-	298	20	0.298	[20]
B,N-CNTs	-	77	16	1.96	[57]
Ni-ACF	774	298	50	0.75	[19]
N-doped PC	2919	77	1	2.71	[52]
Pd-loaded CF	815.6	298	1	0.82	[24]
Pt-doped CA	379	77	22	5.15	[54]
PC	2564.6	77	1	2.67	[55]
Ni-plated PCNF	1310	298	100	2.2	[58]
Ni-loaded ACNF	763.4	298	100	2.12	[32]
Ni-doped ACNF	750.7	298	100	1.39	This work

#### 4. Conclusions

In this study, an in situ doping method based on electrospinning was presented to fabricate hierarchically porous carbon nanofibers with well-dispersed Ni nanoparticles using polyacrylonitrile and pitch as precursors by pre-oxidation, carbonization, and CO<sub>2</sub> activation processes. The effect of Ni doping content on the structure and hydrogen storage performance of porous carbon nanofibers were systematically investigated. We found that nickel doping improved the pore structure and graphitization degree of carbon nanofibers and enhanced the hydrogen adsorption capacity by the spillover effect. When the Ni doping content was 10 wt%, the sample exhibited the highest specific surface area and micropore volume of 750.7 m<sup>2</sup>/g and 0.258 cm<sup>3</sup>/g, respectively. In the hydrogen adsorption/desorption experiments, the sample ACNF-1 presented the best hydrogen storage performance at 298 K and 10 MPa with a storage capacity of 1.39 wt%. This study provides a feasible strategy for the fabrication of carbon-based materials for room-temperature hydrogen storage. However, some limitations of the synthesized material should be noted, such as the low hydrogen storage capacity compared to the DOE target, and the possible agglomeration and fracture of carbon nanofiber at high Ni doping content. Further studies are needed to optimize the synthesis parameters, explore other dopants or modifiers, and evaluate the long-term performance of the material for practical applications.

**Author Contributions:** Conceptualization, F.S.; methodology, L.H.; software, L.H.; validation, H.D., S.Z. and J.Y.; formal analysis, H.D.; investigation, L.H., H.D. and J.Y.; resources, S.Z.; data curation, H.D. and S.Z.; writing—original draft preparation, L.H.; writing—review and editing, F.S.; visualization, L.H.; supervision, F.S.; project administration, F.S.; funding acquisition, F.S. All authors have read and agreed to the published version of the manuscript.

**Funding:** This research was funded by the National Natural Science Foundation of China (No. 12272350) and the National Major Special Program (No. 2017ZX05072005).

**Institutional Review Board Statement:** Not applicable.

**Informed Consent Statement:** Not applicable.

**Data Availability Statement:** The data used to support the findings of this study are available from the corresponding author upon request.

**Acknowledgments:** We would like to express our sincere gratitude to the National Natural Science Foundation of China (No. 12272350) and the National Major Special Program (No. 2017ZX05072005) for their generous financial support for this research. We also thank the staff of the laboratory for their assistance in the experiments and the characterization techniques. We are grateful to the reviewers and editors for their constructive comments and suggestions that helped improve the quality of this paper.

**Conflicts of Interest:** The authors declare no conflict of interest.

## References

1. Cipriani, G.; Di Dio, V.; Genduso, F.; La Cascia, D.; Liga, R.; Miceli, R.; Galluzzo, G.R. Perspective on hydrogen energy carrier and its automotive applications. *Int. J. Hydrogen Energy* **2014**, *39*, 8482–8494. [[CrossRef](#)]
2. Grochala, W. First there was hydrogen. *Nat. Chem.* **2015**, *7*, 264. [[CrossRef](#)] [[PubMed](#)]
3. Abe, J.O.; Popoola, A.P.I.; Ajenifuja, E.; Popoola, O.M. Hydrogen energy, economy and storage: Review and recommendation. *Int. J. Hydrogen Energy* **2019**, *44*, 15072–15086. [[CrossRef](#)]
4. Hosseini, S.E.; Wahid, M.A. Hydrogen from solar energy, a clean energy carrier from a sustainable source of energy. *Int. J. Energy Res.* **2020**, *44*, 4110–4131. [[CrossRef](#)]
5. Yue, M.; Lambert, H.; Pahon, E.; Roche, R.; Jemei, S.; Hissel, D. Hydrogen energy systems: A critical review of technologies, applications, trends and challenges. *Renew. Sustain. Energy Rev.* **2021**, *146*, 111180. [[CrossRef](#)]
6. Sadhasivam, T.; Kim, H.T.; Jung, S.; Roh, S.H.; Park, J.H.; Jung, H.Y. Dimensional effects of nanostructured Mg/MgH<sub>2</sub> for hydrogen storage applications: A review. *Renew. Sustain. Energy Rev.* **2017**, *100*, 523–534. [[CrossRef](#)]
7. Pingkuo, L.; Xue, H. Comparative analysis on similarities and differences of hydrogen energy development in the World's top 4 largest economies: A novel framework. *Int. J. Hydrogen Energy* **2022**, *47*, 9485–9503. [[CrossRef](#)]
8. Demirocak, D.E. *Hydrogen Storage Technologies in Nanostructured Materials for Next Generation Energy Storage and Conversion*; University of Houston: Houston, TX, USA, 2017; pp. 117–142.
9. Zhao, Y.; Gong, M.; Zhou, Y.; Dong, X.; Shen, J. Thermodynamics analysis of hydrogen storage based on compressed gaseous hydrogen, liquid hydrogen and cryo-compressed hydrogen. *Int. J. Hydrogen Energy* **2019**, *44*, 16833–16840.
10. Sorensen, B.; Spazzafumo, G. *Hydrogen and Fuel Cells: Emerging Technologies and Applications*; Academic Press: Cambridge, MA, USA, 2018.
11. Zhang, H.; Zhu, Y.; Liu, Q.; Li, X. Preparation of porous carbon materials from biomass pyrolysis vapors for hydrogen storage. *Appl. Energy* **2022**, *306*, 118131. [[CrossRef](#)]
12. Bicil, Z.; Dogan, M. Characterization of activated carbons prepared from almond shells and their hydrogen storage properties. *Energy Fuels* **2021**, *35*, 10227–10240. [[CrossRef](#)]
13. Isinkaralar, K.; Gullu, G.; Turkyilmaz, A.; Dogan, M.; Turhan, O. Activated carbon production from horse chestnut shells for hydrogen storage. *Int. J. Glob. Warm.* **2022**, *26*, 361–373. [[CrossRef](#)]
14. Hwang, S.I.; Sopher, E.M.; Zeng, Z.; Schulte, Z.M.; White, D.L.; Rosi, N.L. Metal-Organic Frameworks on Palladium Nanoparticle-Functionalized Carbon Nanotubes for Monitoring Hydrogen Storage. *ACS Appl. Nano Mater.* **2022**, *5*, 13779–13786. [[CrossRef](#)]
15. Ren, J.; Zhang, N.; Liu, P. Theoretical Study on Hydrogen Storage Properties of Carbon Aerogels. *Chin. J. Comput. Phys.* **2019**, *36*, 749–756.
16. Meng, Q.; Huang, Y.; Ye, J.; Xia, G.; Wang, G.; Dong, L.; Yang, Z.; Yu, X. Electrospun carbon nanofibers with in-situ encapsulated Ni nanoparticles as catalyst for enhanced hydrogen storage of MgH<sub>2</sub>. *J. Alloys Compd.* **2021**, *851*, 156874. [[CrossRef](#)]
17. Chen, X.; Xue, Z.; Niu, K.; Liu, X.; Lv, W.; Zhang, B.; Li, Z.; Zeng, H.; Ren, Y.; Wu, Y.; et al. Li-fluorine codoped electrospun carbon nanofibers for enhanced hydrogen storage. *RSC Adv.* **2021**, *11*, 4053–4061. [[CrossRef](#)] [[PubMed](#)]
18. Ren, L.; Zhu, W.; Zhang, Q.; Lu, C.; Sun, F.; Liu, X.; Zou, J. MgH<sub>2</sub> confinement in MOF-derived N-doped porous carbon nanofibers for enhanced hydrogen storage. *Chem. Eng. J.* **2022**, *434*, 134701. [[CrossRef](#)]
19. Yadav, A.; Faisal, M.; Subramaniam, A.; Verma, N. Nickel nanoparticle-doped and steam-modified multiscale structure of carbon micro-nanofibers for hydrogen storage: Effects of metal, surface texture and operating conditions. *Int. J. Hydrogen Energy* **2017**, *42*, 6104–6117. [[CrossRef](#)]
20. Kaskun, S.; Kayfeci, M. The synthesized nickel-doped multi-walled carbon nanotubes for hydrogen storage under moderate pressures. *Int. J. Hydrogen Energy* **2018**, *43*, 10773–10778. [[CrossRef](#)]
21. Browning, D.J.; Gerrard, M.L.; Lakeman, J.B.; Mellor, I.M.; Mortimer, R.J.; Turpin, M.C. Studies into the storage of hydrogen in carbon nanofibers: Proposal of a possible reaction mechanism. *Nano Lett.* **2002**, *2*, 201–205. [[CrossRef](#)]
22. Musyoka, N.M.; Wdowin, M.; Rambau, K.M.; Franus, W.; Panek, R.; Madej, J.; Czarna-Juszkiewicz, D. Synthesis of activated carbon from high-carbon coal fly ash and its hydrogen storage application. *Renew. Energy* **2020**, *155*, 1264–1271. [[CrossRef](#)]
23. Sevilla, M.; Mokaya, R.; Fuertes, A.B. Ultrahigh surface area polypyrrole-based carbons with superior performance for hydrogen storage. *Energy Environ. Sci.* **2011**, *4*, 2930–2936. [[CrossRef](#)]

24. Kim, H.; Lee, D.; Moon, J. Co-electrospun Pd-coated porous carbon nanofibers for hydrogen storage applications. *Int. J. Hydrogen Energy* **2011**, *36*, 3566–3573. [[CrossRef](#)]
25. Yodsin, N.; Sakagami, H.; Udagawa, T.; Ishimoto, T.; Jungstittiwong, S.; Tachikawa, M. Metal-doped carbon nanocones as highly efficient catalysts for hydrogen storage: Nuclear quantum effect on hydrogen spillover mechanism. *Mol. Catal.* **2021**, *504*, 111486. [[CrossRef](#)]
26. Jeong, J.H.; Kim, B.H. Low-cost effective photocatalytic activity under visible light of pitch-based porous carbon nanofiber composites aided by zinc oxide. *Synth. Met.* **2019**, *247*, 163–169. [[CrossRef](#)]
27. Ge, J.C.; Wu, G.; Yoon, S.K.; Kim, M.S.; Choi, N.J. Study on the Preparation and Lipophilic Properties of Polyvinyl Alcohol (PVA) Nanofiber Membranes via Green Electrospinning. *Nanomaterials* **2021**, *11*, 2514. [[CrossRef](#)] [[PubMed](#)]
28. Nguyen, T.D.; Lee, J.S. Electrospinning-Based Carbon Nanofibers for Energy and Sensor Applications. *Appl. Sci.* **2022**, *12*, 6048. [[CrossRef](#)]
29. Plerdsranoy, P.; Thaweelap, N.; Poo-arporn, Y.; Khajondetchairit, P.; Suthirakun, S.; Fongkaew, I.; Chanlek, N.; Utke, O.; Pangon, A.; Utke, R. Hydrogen adsorption of O/N-rich hierarchical carbon scaffold decorated with Ni nanoparticles: Experimental and computational studies. *Int. J. Hydrogen Energy* **2021**, *46*, 5427–5440. [[CrossRef](#)]
30. Kuang, M.; Guan, A.; Gu, Z.; Han, P.; Qian, L.; Zheng, G. Enhanced N-doping in mesoporous carbon for efficient electrocatalytic CO<sub>2</sub> conversion. *Nano Res.* **2019**, *12*, 2324–2329. [[CrossRef](#)]
31. Kim, S.H.; Kim, B.H. Influence of boron content on the structure and capacitive properties of electrospun polyacrylonitrile/pitch-based carbon nanofiber composites. *Synth. Met.* **2018**, *242*, 1–7. [[CrossRef](#)]
32. Thaweelap, N.; Plerdsranoy, P.; Poo-arporn, Y.; Khajondetchairit, P.; Suthirakun, S.; Fongkaew, I.; Hirunsit, P.; Chanlek, N.; Utke, O.; Pangon, A.; et al. Ni-doped activated carbon nanofibers for storing hydrogen at ambient temperature: Experiments and computations. *Fuel* **2021**, *288*, 119608. [[CrossRef](#)]
33. Gao, Z.; Ding, C.; Wang, J.; Ding, G.; Xue, Y.; Zhang, Y.; Zhang, K.; Liu, P.; Gao, X. Cobalt nanoparticles packaged into nitrogen-doped porous carbon derived from metal-organic framework nanocrystals for hydrogen production by hydrolysis of sodium borohydride. *Int. J. Hydrogen Energy* **2019**, *44*, 8365–8375. [[CrossRef](#)]
34. Huang, Y.; Yan, H.; Zhang, C.; Wang, Y.; Wei, Q.; Zhang, R. Interfacial Electronic Effects in Co@N-Doped Carbon Shells Heterojunction Catalyst for Semi-Hydrogenation of Phenylacetylene. *Nanomaterials* **2021**, *11*, 2776. [[CrossRef](#)] [[PubMed](#)]
35. Fan, L.; Du, X.; Zhou, S.; Yang, P.; Li, M.; Kang, Z.; Guo, H.; Fan, W.; Kang, W.; Zhang, L.; et al. Efficient platinum harvesting of MOF-derived N-doped carbon through cathodic cyclic voltammetry for hydrogen evolution. *Electrochim. Acta* **2019**, *317*, 173–181. [[CrossRef](#)]
36. Xu, Y.; Cheng, Y.; Jia, Y.; Ye, B.C. Synthesis of MOF-derived Ni@C materials for the electrochemical detection of histamine. *Talanta* **2020**, *219*, 121360. [[CrossRef](#)]
37. Guo, L.; Hao, L.; Zhang, Y.; Yang, X.; Wang, Q.; Wang, Z.; Wang, C. Metal-organic framework precursors derived Ni-doping porous carbon spheres for sensitive electrochemical detection of acetaminophen. *Talanta* **2021**, *228*, 122228. [[CrossRef](#)]
38. Yadav, A.; Verma, N. Enhanced hydrogen storage in graphitic carbon micro-nanofibers at moderate temperature and pressure: Synergistic interaction of asymmetrically-dispersed nickel-ceria nanoparticles. *Int. J. Hydrogen Energy* **2017**, *42*, 27139–27153. [[CrossRef](#)]
39. Weng, Q.; Zeng, L.; Chen, Z.; Han, Y.; Jiang, K.; Bando, Y.; Golberg, D. Hydrogen Storage in Carbon and Oxygen Co-Doped Porous Boron Nitrides. *Adv. Funct. Mater.* **2021**, *31*, 2007381. [[CrossRef](#)]
40. Liu, Y.; Li, D.; Lin, B.; Sun, Y.; Zhang, X.; Yang, H. Hydrothermal synthesis of Ni-doped hierarchically porous carbon monoliths for hydrogen storage. *J. Porous Mater.* **2015**, *22*, 1417–1422. [[CrossRef](#)]
41. Wei, W.; Wang, F.; Yang, J.; Zou, J.; Li, J.; Shi, K. A superior potassium-ion anode material from pitch-based activated carbon fibers with hierarchical pore structure prepared by metal catalytic activation. *ACS Appl. Mater. Interfaces* **2021**, *13*, 6557–6565. [[CrossRef](#)]
42. Yang, C.R.; Tseng, S.F.; Chen, Y.T. Characteristics of graphene oxide films reduced by using an atmospheric plasma system. *Nanomaterials* **2018**, *8*, 802.
43. Peng, Z.; Xu, Y.; Luo, W.; Wang, C.; Ma, L. Conversion of biomass wastes into activated carbons by chemical activation for hydrogen storage. *ChemistrySelect* **2020**, *5*, 11221–11228. [[CrossRef](#)]
44. Hernández-Vázquez, E.E.; Muñoz, F.; López-Moreno, S.; Morán-López, J.L. First-principles study of Ni adatom migration on graphene with vacancies. *RSC Adv.* **2019**, *9*, 18823–18834. [[CrossRef](#)] [[PubMed](#)]
45. Li, Y.; Xu, Y.; Liu, Y.; Pang, H. Exposing {001} crystal plane on hexagonal Ni-MOF with surface-grown cross-linked mesh-structures for electrochemical energy storage. *Small* **2019**, *15*, 1902463. [[CrossRef](#)] [[PubMed](#)]
46. Thommes, M.; Kaneko, K.; Neimark, A.V.; Olivier, J.P.; Rodriguez-Reinoso, F.; Rouquerol, J.; Sing, K.S. Physisorption of gases, with special reference to the evaluation of surface area and pore size distribution (IUPAC Technical Report). *Pure Appl. Chem.* **2015**, *87*, 1051–1069. [[CrossRef](#)]
47. Xiao, Y.; Zheng, X.; Chen, X.; Jiang, L.; Zheng, Y. Synthesis of Mg-doped ordered mesoporous Pd–Al<sub>2</sub>O<sub>3</sub> with different basicity for CO, NO, and HC elimination. *Ind. Eng. Chem. Res.* **2017**, *56*, 1687–1695. [[CrossRef](#)]
48. Liu, C.; Xiao, N.; Li, H.; Dong, Q.; Wang, Y.; Li, H.; Wang, S.; Zhang, X.; Qiu, J. Nitrogen-doped soft carbon frameworks built of well-interconnected nanocapsules enabling a superior potassium-ion batteries anode. *Chem. Eng. J.* **2020**, *382*, 121759. [[CrossRef](#)]
49. Huang, J.; Liang, Y.; Dong, H.; Hu, H.; Yu, P.; Peng, L.; Zheng, M.; Xiao, Y.; Liu, Y. Revealing contribution of pore size to high hydrogen storage capacity. *Int. J. Hydrogen Energy* **2018**, *43*, 18077–18082. [[CrossRef](#)]

50. Lee, H.M.; Heo, Y.J.; An, K.H.; Jung, S.C.; Chung, D.C.; Park, S.J.; Kim, B.J. A study on optimal pore range for high pressure hydrogen storage behaviors by porous hard carbon materials prepared from a polymeric precursor. *Int. J. Hydrogen Energy* **2018**, *43*, 5894–5902. [[CrossRef](#)]
51. Im, J.S.; Park, S.J.; Kim, T.J.; Kim, Y.H.; Lee, Y.S. The study of controlling pore size on electrospun carbon nanofibers for hydrogen adsorption. *J. Colloid Interface Sci.* **2008**, *318*, 42–49. [[CrossRef](#)]
52. Wang, Z.; Sun, L.; Xu, F.; Zhou, H.; Peng, X.; Sun, D.; Wang, J.; Du, Y. Nitrogen-doped porous carbons with high performance for hydrogen storage. *Int. J. Hydrogen Energy* **2016**, *41*, 8489–8497. [[CrossRef](#)]
53. Conte, G.; Policicchio, A.; De Luca, O.; Rudolf, P.; Desiderio, G.; Agostino, R.G. Copper-doped activated carbon from amorphous cellulose for hydrogen, methane and carbon dioxide storage. *Int. J. Hydrogen Energy* **2022**, *47*, 18384–18395. [[CrossRef](#)]
54. Singh, S.; Bhatnagar, A.; Dixit, V.; Shukla, V.; Shaz, M.A.; Sinha, A.S.K.; Srivastava, O.N.; Sekkar, V. Synthesis, characterization and hydrogen storage characteristics of ambient pressure dried carbon aerogel. *Int. J. Hydrogen Energy* **2016**, *41*, 3561–3570. [[CrossRef](#)]
55. Balderas-Xicohtencatl, R.; Schlichtenmayer, M.; Hirscher, M. Volumetric hydrogen storage capacity in metal–organic frameworks. *Energy Technol.* **2018**, *6*, 578–582. [[CrossRef](#)]
56. Hwang, S.H.; Kim, Y.K.; Seo, H.J.; Jeong, S.M.; Kim, J.; Lim, S.K. The enhanced hydrogen storage capacity of carbon fibers: The effect of hollow porous structure and surface modification. *Nanomaterials* **2021**, *11*, 1830. [[CrossRef](#)] [[PubMed](#)]
57. Sawant, S.V.; Banerjee, S.; Patwardhan, A.W.; Joshi, J.B.; Dasgupta, K. Synthesis of boron and nitrogen co-doped carbon nanotubes and their application in hydrogen storage. *Int. J. Hydrogen Energy* **2020**, *45*, 13406–13413. [[CrossRef](#)]
58. Kim, B.J.; Lee, Y.S.; Park, S.J. A study on the hydrogen storage capacity of Ni-plated porous carbon nanofibers. *Int. J. Hydrogen Energy* **2008**, *33*, 4112–4115. [[CrossRef](#)]

**Disclaimer/Publisher’s Note:** The statements, opinions and data contained in all publications are solely those of the individual author(s) and contributor(s) and not of MDPI and/or the editor(s). MDPI and/or the editor(s) disclaim responsibility for any injury to people or property resulting from any ideas, methods, instructions or products referred to in the content.